Layer-by-layer functionalized nanotube arrays: A versatile microfluidic platform for biodetection

Allison L. Yost, Setareh Shasavari, Grinia M. Bradwell, Roberta Polak, Fabio Fachin, Robert E. Cohen, Gareth H. McKinley, Mehmet Toner, Michael F. Rubner, Brian L. Wardle

ABSTRACT

Here, we demonstrate layer-by-layer (LbL) assembly of polyelectrolyte multilayers (PEM) on three-dimensional nanofiber scaffolds. High porosity (99%) aligned carbon nanotube (CNT) arrays are photolithographically patterned into elements that act as textured scaffolds for the creation of functionally-coated (nano)porous materials. Nanometer-scale bilayers of Poly(allylamine hydrochloride)/Poly(styrene sulfonate) are formed conformally on the individual nanotubes by repeated deposition from aqueous solution in microfluidic channels. Computational and experimental results demonstrate that the LbL deposition is dominated by diffusive transport of the polymeric constituents, and we use this understanding to demonstrate spatial tailoring on the patterned nanoporous elements. A proof-of-principle application, microfluidic bioparticle capture using NHS-biotin binding for isolation of prostate specific antigen (PSA), is demonstrated.

The ability to achieve nanoscale control of interfaces and surfaces has fueled new ideas and technologies in a myriad of applications, including the design of various microelectronic [1-3], energy storage [4-7], optical [8-11], and biomedical devices [12-15]. In particular, biomedical research has benefited from advances in nanoscale surface chemistry and surface manipulation, enabling applications from controllable adsorption/release of proteins to affinity chromatography to drug delivery [16-18]. The vast majority of surface tailoring however, has been demonstrated on readily accessible planar or particle surfaces and the transition to more complex 3D porous materials, particularly space-constrained nanoporous materials, is currently limited. Thus, what is clearly needed to produce the next generation of biomedical devices, is the ability to systematically functionalize the surfaces of 3D nanotemplates contained within complex geometries with conformal nanoscale coatings of any desired chemistry and surface morphology. The conformality of the resultant coating and its precise nanoscale thickness control is critical to maintaining the advantages and functionality provided by the original 3D nanoscale template.

A promising nanostructuring approach to create 3D templates is the use of textured nanoporous elements as a scaffold for surface functionalization and as building blocks for various devices. One such textured element that has received considerable attention is an aligned array of nanofibers, such as carbon nanotubes

(CNTs) [19, 20, 21]. CNTs are attractive due to their intrinsic mechanical, electrical, magnetic, and optical properties [22-29], as well as the multiple routes to synthesize and give texture to bulk assemblies of the nanofibers. Biomedical applications are particularly well suited due to the wealth of existing surface chemistries available for functionalization (e.g., antibody binding). As such, one can apply nanoscale control over chemical composition, spatial morphology, and the interfaces of materials to create versatile, materials-driven platform technologies that can be targeted to a wide range of applications. For example, by exploiting the porosity (99%) of CNT arrays, vertically aligned carbon nanotube (VACNT) forests can be successfully integrated into a variety of devices [30, 31] including within microfluidic devices, allowing separation and specific targeting of biomolecules ranging from sizes of 40nm-10μm with an enhanced capture efficiency of 7x [32, 33]. Due to their size and high surface area, CNTs provide unique accessibility to bioparticles in a high throughput fashion at scales currently difficult to achieve through MEMs at such rates, such as biomarker proteins, viruses, exosomes, or cell-free DNA in blood or other bodily fluids for diagnostics applications.

Although in principle, various approaches exist for modifying the surfaces of carbon nanotubes contained within CNT arrays, the layer-by-layer (LbL) assembly approach [34] holds the most promise for fulfilling the multiple requirements of nanoscale thickness and morphology control, conformal coating ability and the ability to create a wide range of different surface chemistries and functionalities. Indeed, the greatest advantage of the LbL assembly process compared to other coating processes continues to be its ability to produce nanoscale conformal coatings from an extremely wide variety of organic, inorganic and biological molecules and materials [35-38]. Excellent examples of these capabilities as applied to biomaterial based devices and constructs including sensors [39] and drug delivery elements [40, 41] abound in the literature. Relevant to this work is the idea that LbL assembly can be readily carried out within the confines of complex nanoscale geometries and within functional microfluidic devices [42]. In the former case, LbL assembly has been demonstrated within nanochannels and nanopores [42-46]. In the latter case, LbL assembled coatings have been used for the development of microfluidic based *in vitro* assays or for studying fundamental cell and tissue biology. For example, Sung et al. modified PDMS surfaces using LbL coatings to reduce non-specific binding and for enhanced detection of low levels of protein [47]. Others have designed a microfluidic platform with LbL coatings for identifying the dengue virus using an ELISA approach. Results indicated that LbL coatings on channel surfaces improved stability and efficiency, reducing surface modification time twelve-fold [48]. Alternatively, LbL modified microfluidic systems have been used to control the flow or flow constituents within the device. Kirchof et al., for example, utilized LbL coatings in microfluidic devices to generate pH gradients that promote cell migration [49], while Barker et al. used them to alter surface charge and control the direction of electroosmotic flow [50].

Our approach has been to utilize LbL coatings as a means to systematically functionalize patterned carbon nanotube arrays contained within microfluidic

devices designed to filter, capture and detect low levels of biological markers for disease [32,33]. We demonstrate that it is possible to control the LbL assembly pattern within a microfluidic device by only varying the height of the microchannel. In this manner, we can coat and functionalize individual carbon nanotubes throughout the entire CNT array or just cover the outer surface of the array. In the former case, conformal coatings on individual nanotubes have been achieved within arrays with tube-to-tube spacings of about 80 nm. This level of functionalization control can be used to take full advantage of the highly porous nature of the CNT arrays, as well their ability to controllably capture and release biomarkers of various types. To demonstrate this, we have used this technology to functionalize the CNT surfaces with antibodies and capture prostate specific antigen (PSA) as an exemplary capture target. A significant challenge in microfluidic platform bioparticle isolation is to achieve sufficient interaction between the target biomolecule and the functional surfaces to promote binding. This work provides a powerful tool to functionally tailor and grade nanomaterials in 3 dimensions, enabling the design of devices that enhance bioparticle-surface interaction. Additionally, due to the nature of the spacing between individual CNTs (~80 nm), this platform specifically has high potential in isolation of nano-sized bioparticles, such as viruses, exosomes, or DNA.

The microfluidic chip design and assembling processes (Fig 1) were developed to favor adsorption and LbL conformal coating on the nanoporous CNT elements contained within the microfluidic device (Fig 1a). Patterned CNT elements were grown via chemical vapor deposition (CVD) on Si wafers. These porous VACNT forests consist of arrays of multi-walled CNTs (OD 7.78 +/- 0.85 nm, ID 5.12 nm +/- 0.76 nm, spaced ~80 nm apart, # walls 5 +/- 1, 1 vol%, 1.59 g/cm^3 [51, 52]) (Fig. 1b,c) patterned using photolithography into macroscopic elements that have high porosity (~99%) and accessibility to aqueous solutions. For this study, one geometric pattern of CNTs was used for simplicity: a single pillar with 1mm diameter (consisting of more than 10^8 individual carbon nanutubes) centered in the 3 mm wide, 7 mm long microfluidic channel (Fig 1b, c). CNT pillar heights averaged 50 μm tall, but ranged between 30-80 μm. Results were also obtained with other element geometries (not shown), such as an array of pillars or a "wall", i.e. rectangular feature perpendicular to flow. In fact, for particle isolation, a wall device, which acts like a filter, would be an ideal design; however, the resulting pressure drop can damage the adhesion of the CNTs to the substrate. Therefore, the geometric design involves the trade-off between the maximum allowed pressure and maximum interception of flow streamlines with the CNT elements. Photolithography permits numerous patterns to be designed in the future for further investigation of an optimized CNT element geometry.

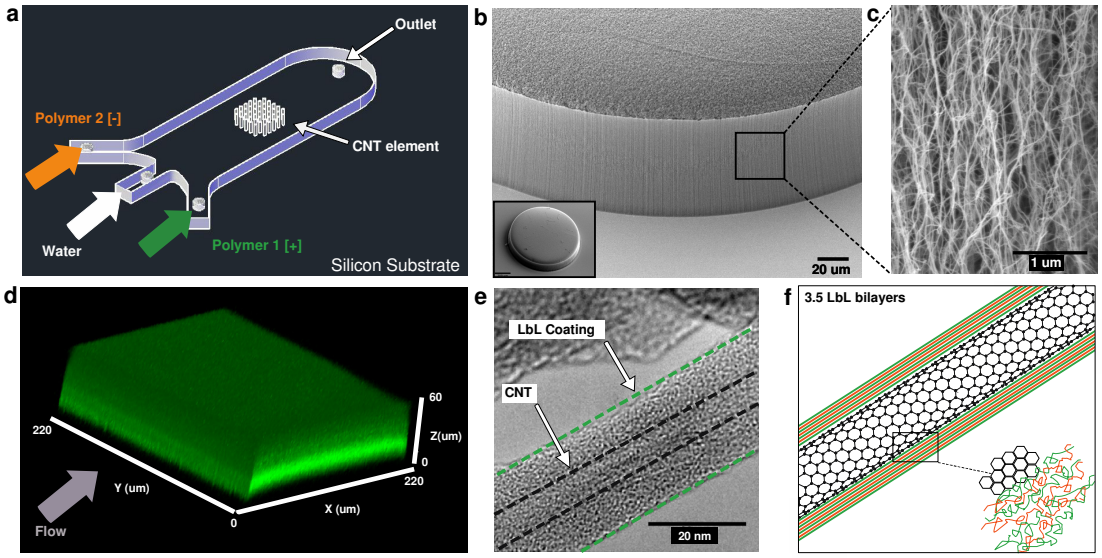

Figure 1: Schematic and characterization of LbL coating on nanoporous CNT element
(a) Illustration of microfluidic chip design featuring pillar (D = 1 mm) CNT element in microfluidic channel (3 mm wide)(b) SEM images of an as-grown aligned CNT pillar element (c) High resolution SEM of CNT element exhibiting textured porosity (d) 3D reconstruction of confocal z-slices (PAH-Fluor, 488 nm) of a 220 µm x 220 µm section of CNT pillar element, demonstrating polymer coating through z plane. (e) TEM micrograph of individual CNT coated with 3.5 bilayers of PAH-Fluor/SPS assembled at pH 9.3. Dashed black line outlines CNT diameter, and green dashed line indicates outer edge of LbL coating as depicted in the (f) illustration of 3.5 LBL multilayers.

Microfluidic channels were fabricated following standard soft lithography protocols [53] in conjunction with negative molds made of SU-8 photoresist (Microchem, MA) onto silicon wafers. The microfluidic chip design has three inlets: one for each polyelectrolyte solution used in the LbL process and one for a water rinse required to wash out the polymer molecules that are not adsorbed to the CNTs (Fig. 1a).

Polyelectrolyte multilayer film (PEM) deposition on the CNT surfaces was performed via LbL assembly of poly(allylamine hydrochloride) (PAH) [15 kDa] and poly(styrene sulfonate) (SPS) [70 kDa], within the microfluidic devices. PAH conjugated with fluorescein, PAH-Fluor, was used to permit visualization. Integrated CNT microfluidic devices were primed with a negatively charged surfactant (sodium dodecyl benzene sulfonate (SDBS)), selected for its propensity to bind to individual CNTs [54] and for its electrical charge that favors polyelectrolyte adsorption. Because CNTs have a tendency to be innately hydrophobic, the SDBS served to lower the surface tension, making the CNT elements more hydrophilic and more receptive to polymer coating [55-56]. After priming, devices were rinsed with DI water for 5 minutes at 6 µL /min and LbL assembly was performed via alternate flow of PAH-Fluor and SPS solutions at 6 µL /min for 5 minutes each, with

intermediate water rinse flow (5 min, 6 μL /min). PAH-Fluor was the first and last layer deposited.

As previously described, PAH/SPS films assembled at pH 9.3 present primary amine groups isolated in hydrophobic pockets which can be can be opened via an acid treatment that will protonate the amine groups and expose them to the surface of the film. [57, 58]. The exposed amine groups can be reacted with selected chemistries; such as N-Hydroxysuccinimide (NHS) groups creating stable amide bonds to link a biotinylated surface on the film surface [59]. Thus, pH 9.3 was selected for standard LbL assembly, and an acid treatment at pH 2.5 was performed post-LbL and prior to the bioparticle capture protocol to generate amine-rich surfaces. LbL assembly was performed successfully with 3.5 bilayers of PAH-Fluor/SPS at pH 9.3 via continuous flow LbL assembly.

Toward our goal of developing a method for on demand functional coating at the nanoscale with complete morphology control, we first sought to achieve full, uniform coating throughout the entire 1 mm pillar CNT device. Full CNT pillar element coating was achieved when devices were fabricated such that there was a gap (~50 μm) between the CNT element height and the PDMS channel height. Confocal microscopy images showed polymer coating throughout the entire volume of the CNT element [Fig. 1d] and TEM micrographs suggest nanoscale conformal coating layers on individual CNTs within the element by comparing CNT diameters before and after LbL [Fig. 1e], confirming the ability to coat the individual CNTs and construct a 3-dimensional LbL coated surface. It is notable that there tends to be a higher intensity of fluorescent signal in the mid z-plane of the device consistent in results, as shown in [Fig. 1d], suggesting a larger amount of coating in that location. We believe this is an artifact of the rinsing methods used, which removes some polymer from the top surface of the device. Additionally, it is possible that this intensity variation is diagnostic of the CNT morphology, and perhaps changes in CNT density in the z-plane yield changes in polymer coating. It is also possible that it is due to an imaging artifact, based on utilizing a confocal to image through the PDMS channel, which causes scattering and difficulty in focusing.

Because uniform, conformal coating was achieved with a gap in the device geometry, we hypothesized that the presence of this gap was important in controlling the coating morphology. To test that hypothesis, we then designed devices such that there was no gap between the CNTs and the top of the PDMS channel, by slightly compressing the CNT element along the z-axis (reference axis in Fig. 1d). Results showed an annular coating of the CNTs with this device geometry. The thickness of the annular coating ring was on the order of half the height of the CNT element. This annular coating mechanism was maintained throughout the volume of the CNT element, and was distinctly different from the full coating results when a gap was present [Fig. 2c, d]. Thus, by changing the geometry of the device elements, we can exhibit spatial control of LbL coating. Furthermore, methods have been investigated to close a PDMS gap in situ, such that the channel could be sealed prior to any biological or chemical assay, but after the desired LbL coating design

could be performed [60]. This opens the doors to microfluidic devices with various coating designs and geometries for functional surfaces, without compromising a large portion of the fluid potentially bypassing the functional surfaces, or wasting a large portion of a precious biological sample, which a gap may allow.

To describe the difference in uniform vs. annular coating mechanisms, a three-dimensional numerical model was developed in COMSOL Multiphysics 4.4 to investigate the transport of the polymer solution through the CNT elements. The transport phenomena involved in the experiments were convection, diffusion, and adsorption. In our numerical model, we included convection and diffusion, neglecting adsorption since the time scale for the adsorption is much smaller than that of diffusion [61]. Experimental observations suggested that as soon as the polymer solution is diffused into the CNT forest, the polymer is adsorbed onto the CNT surface. To further quantify the kinetics of the adsorption, we can calculate the Damköhler number, Dk, which compares the reaction rate with the rate of diffusive transport, [62]:

$$Dk = \frac{\text{time scale of diffusion}}{\text{time scale of reaction}}$$

Here the reaction is in fact the adsorption of the long-chained polymer molecules with charged groups to the surface with opposite polarity. Based on the theoretical analysis by Stuart et al. [61], equilibrium in adsorption should be attained in a time scale of seconds in our system. In our experiments, the diffusion occurs in a time scale of minutes to hours, therefore, the Damköhler number is in the range of 100-1000, which justifies neglecting the adsorption kinetics in the numerical model.

For quantitative comparison of the rate of the polymer transport by advection and diffusion, we determined the Péclet number, defined as

$$Pe = U_c L_c / D_{12},$$

where U_c and L_c are characteristic velocity and length scale respectively and D_{12} denotes the binary diffusion coefficient of species 1 (polymer) and solvent 2 (water). In our system, there exist two Péclet numbers since we have two different velocities as a result of different structural length scales: one the height of the microchannel and the other is the pore size in the CNT forest. Inside the porous domain, the characteristic velocity can be obtained from comparing the hydrodynamic resistances of the porous pillar and the side gap between the pillar and the channel wall. The order of magnitude for the average velocity through the side gap can be estimated as $U \sim \frac{H^2}{\mu}\frac{\Delta p}{L}$, where H is the channel height, μ is the fluid viscosity, and $\Delta p/L$ is the pressure drop over the length of the channel, L. Also, based on Darcy's law, the apparent velocity in the porous CNT forest is $U_p = \frac{\kappa}{\mu}\frac{\Delta p}{L}$, where κ is the permeability of the CNT forest. Therefore, the ratio of the two

velocities is $\frac{U_p}{U} = \frac{\kappa}{H^2} = 10^{-8}$ (using $H = 100\,\mu m$ and $\kappa \sim 10^{-16}\,m^2$, derived from [63]). In our experiments the channel flow velocity is $U = 3 \times 10^{-4}\,m/s$ (corresponding to a flow rate of 6 $\mu l/min$ through the microchannel) and the binary diffusion coefficient is $D_{12} = 10^{-11}\,\frac{m^2}{s}$ [64]. Therefore, the Péclet number in the channel is $Pe = \frac{UH}{D_{12}} = 3 \times 10^3$ while that in the CNT forest is $Pe_p = \frac{U_p H}{D_{12}} = 3 \times 10^{-5}$, which clearly shows that outside the porous CNT pillar, convection is dominant while, inside the CNTs, diffusion controls the transport of polymer molecules in spite of the high porosity (%99) of the CNTs.

In fact the flow permeation inside the pillar is negligible as a result of two contributing factors: i) the low Darcy number, Da, defined as the permeability non-dimensionalized by the porous collector diameter, D:

$$Da = \frac{\kappa}{D^2},$$

yields a value of $Da = 10^{-10}$ for our system, and ii) the low confinement ratio, the ratio of the collector diameter ($1\,mm$) to the channel width ($3\,mm$). The flow permeation through confined cylindrical porous collectors is studied by Shahsavari et al. in [65], according to which the superficial velocity in the porous region relative to the free stream velocity should be in the order of 10^{-8} for our geometrical parameters, which is the same result as we estimate from comparing the hydrodynamic resistance of the channel and the porous CNT pillar. Ultimately, the combination of these two factors suggests that the porous CNT collector is essentially impermeable via convection.

The resulting concentration distributions based on numerical modeling (Fig. 2c, d) were consistent with the experimental findings, and explain the two separate and distinct coating patterns observed experimentally [Fig. 2a, b]. Ultimately, the numerical modeling confirmed that the assembly process is dominated by diffusion, where results yielded different coatings as in the device with a gap on top of the pillar, the polymer molecules diffuse (downwards) through a thickness of ~50 μm, while in the device with no gap, the polymer molecules can only diffuse radially. Experimental results showed that this radial, annular coating was on the order of 50 μm as well. Additionally, while the assembly process is diffusion dominated, the use of a microfluidic system adds value, not in the coating mechanism, but in specificity. By providing a constant flow during the assembly process, a large amount of nonspecific adsorbed material was removed from the channel, yielding enhanced analysis.

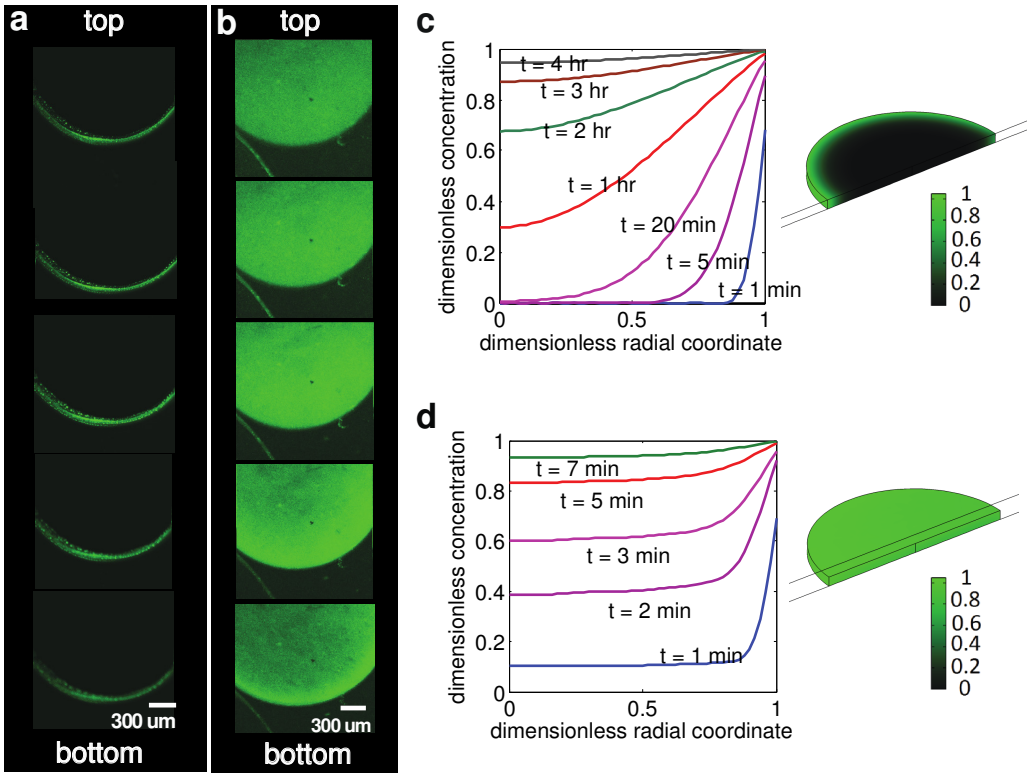

Figure 2: Spatial control of LbL multilayer deposition (a) confocal z-slices in 10 µm increments of a section of CNT device with no gap in microchannel (PEM assembly performed with $(PAH9.3/SPS9.3)_{3.5}$). (b) confocal z-slices in 10 µm increments of a section of CNT device with a 50 µm gap in microchannel (PEM assembly performed with $(PAH9.3/SPS9.3)_{3.5}$). (c) 3D numerical simulation of polymer concentration for no gap device after 5 min. flow of polymer solutions and (d) 3D numerical simulation of polymer concentration for gap device after 5 min flow of polymer solutions.

We used this technology to functionalize the CNT surfaces with antibodies and capture prostate specific antigen (PSA) as an exemplary capture target. A modified sandwich enzyme-linked immunosorbent assay (ELISA) on circular cross-section aligned CNT element devices with 3.5 bilayers was performed to capture prostate specific antigen (PSA) (100 ng/mL), using a biotinylated secondary antibody and streptavidin coated quantum dots (605 nm) [Fig 3a]. All capture and control experiments were performed on devices with a gap, thus employing a full spatial LbL coating. Based on confocal microscopy, results indicate high correlation between LbL coating signal (FITC, 488nm) and capture signal (Qdots, 605 nm) with capture observed throughout the volume of the device (through z plane) [Fig. 3b]. This is particularly advantageous for particle capture, as the commonly used approach in microfluidics limits capture to solely the element outer surface, rather than through the entire element volume as shown here. Intensity measurements were taken across devices and in multiple z-plane stacks using ImageJ and the average ratio of signal to background noise was determined. The LbL functionalization approach yields capture 1.4 times higher than all CNT element

controls, which demonstrates that specific, covalent capture was achieved within the CNT elements.

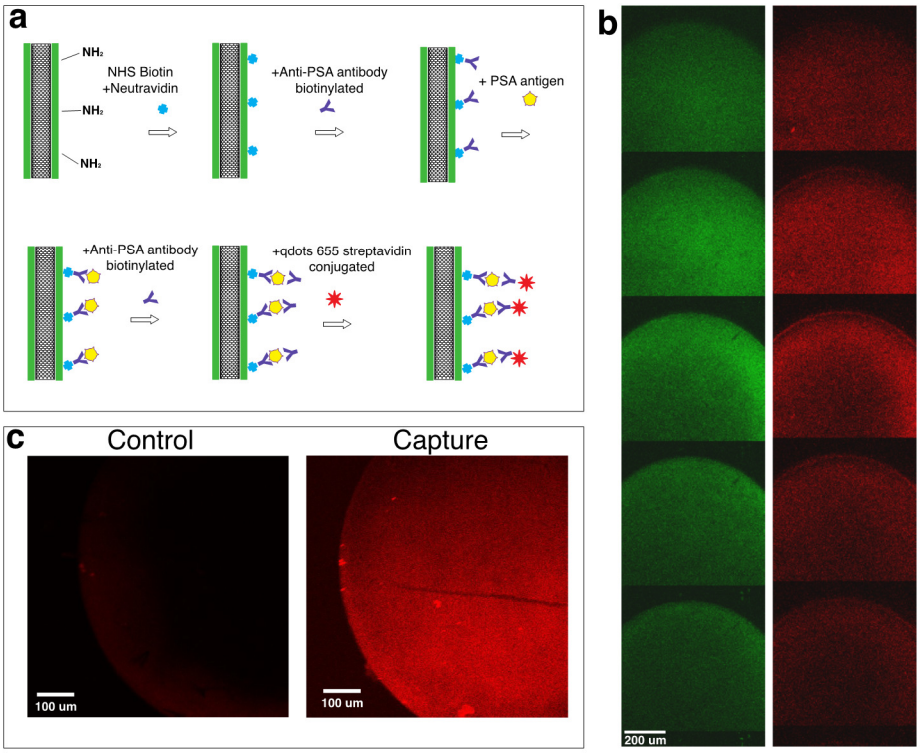

Figure 3: Bioparticle capture utilizing functionalized LbL coated nanoporous element. (a) Illustration of capture protocol used for PSA (100 ng/mL) capture. Acid treatment after LbL assembly protonates and exposes reactive amine groups. The film is then reacted with the desired chemistries to achieve PSA capture and detection by using quantum dots. (b) Confocal z-slices in 15 µm increments (starting from bottom of microfluidic channel) of a section of CNT pillar element, demonstrating both LbL coating (green, FITC, 488 nm) and capture (red, Qdot, 605 nm) (c) a mid-plane z-slices of control (left) and capture (right) devices at average intensities from multi-device series. Control experiment consists of rinsing LbL device with blocking buffer, and then proceeding directly to incubating with quantum dots.

Although the PSA concentrations used here are not in the relevant range levels encountered in current assays found in the literature (e.g. ≤ 0.1 ng/mL)[66], the capture protocol demonstrates the broad utility of the 3D LbL coating platform on CNT elements. Designing devices with sufficient physical interaction between bioparticle targets and the functionally coated surfaces is a great challenge in microfluidic bioparticle isolation. By using this platform, we increase the surface area by a factor of 20 for an equivalent channel volume with planar LbL coating, providing an enhanced sensing platform that is compatible with current microfluidic platforms.

Due to the conformality of the LbL coating, this approach can be used to control the intra-CNT spacing within the 3D element, enabling further isolation flexibility by serving as a design tool. As demonstrated by Fachin et al [33], the CNT forests allow isolation of particles over three orders of magnitude in size using a single chip: particles that are larger than the average inta-CNT spacing (~80nm) do not penetrate the CNT elements and can be isolated on the features' external surfaces either via mechanical filtration or via chemical affinity; particles that are smaller than the average intra-CNT spacing penetrate the forest and can be isolated on the forests' internal surfaces using biomolecular recognition. This dual mechanism displayed by a single structure combined with our new ability to change the intra-CNT spacing via LbL on the nanoscale allows for the possibility of simultaneous multi-scale separation across even larger bioparticle size ranges, specifically providing a tool to access particles on the scale <80 nm, such as viruses, proteins, and exosomes.

Our model suggests that changing the CNT elements geometry to optimize the flow interception at a given pressure drop and fluid volumetric flow rate enhances polymer and bioparticle interception with the CNT surfaces. Additionally, we believe our recorded intensity via confocal imaging is conservative and may underestimate result significance: due to the fabrication technique of the microfluidic devices, imaging must be performed upside-down, through the PDMS because of the opacity of silicon. In addition, the PDMS cap can vary in thickness depending on soft lithography fabrication. Thus, there is higher variability across light intensity data due to reflection of excitation light from the Silicon substrate and light scattering through the PDMS cap. Thus, future work may focus on changing the CNT element shape and substrate used for fabrication or configuration necessary for imaging to increase device repeatability. One possibility for enhancement is to utilize quartz [67, 68] rather than silicon as the base substrate, which would allow for imaging through the bottom of the device and avoid light reflection or PDMS light scattering.

A key future application of the materials and technique demonstrated here is to enhance capture in microfluidic devices by enhancing interaction with 3D functionalized surfaces, rather than planar surfaces, and to enhance capture and detection of nano-scale bioparticles, such as viruses (<100 nm), exosomes (30-100 nm) or rare proteins (~10nm) containing important information about disease state and progression. As a first step towards this goal, we have demonstrated PEM coating on individual CNT using PAH-Fluor and SPS. Additionally, using this method, two unique coating patterns can be achieved, depending on device geometry, which demonstrates an understanding and control over coating morphology. By fabricating devices with a gap between the CNT element and the PDMS, full, conformal PEM coating results. By ensuring no gap exists between the CNT element and the PDMS channel, an annular coating is achieved. These unique coating results can be used for different design criteria and applications. Finally, it was demonstrated that using these PEMs, individual CNTs can be functionalized for bioparticle capture.

The wide-ranging functionality of assembly materials makes it possible to tailor, at the nanoscale, physical properties including the mechanical, electrical, and optical properties of the coatings, as well a as chemical functionality. While work here demonstrates this capability using A-CNT (textured) scaffolds, the technique developed may be applied to other nanoporous material scaffolds, such as carbon nanofibers, nanowires, or aerogels, to control interfaces and surfaces in 3D and bulk configurations.

Methods

CNT and device fabrication:

Vertically aligned carbon nanotubes (VACNTs) were grown in a 22 mm inner diameter quartz tube furnace at atmospheric pressure via chemical vapor deposition [69, 70]. Growth takes place at a nominal temperature of 750 C, with ethylene as the carbon source. VACNTs were grown on <100> 6-inch Si substrates (p-type, 1-10 OHM cm, Silicon Quest International) with a catalyst layer composed of 1 nm Fe/10 nm Al2O3 via electron beam deposition. The nanotubes grown using this method are multi-walled (concentric walls) with an average diameter of ~8 nm, average intra-CNT spacing of ~80 nm, leading to a volume fraction of less than 1% CNTs. CNT height averaged 50 μm tall, but ranged between 30-80 μm. Height is primarily a function of growth time, though small changes in environmental conditions affect growth. Catalyst areas are defined by photoresist photolithography.

To fabricate the microfluidic channel, a 10:1 mixture of polydimethylsiloxane (PDMS) pre-polymer and curing agent (Sylguard 184, Dow Corning, MI) was poured onto a photolithographically patterned SU-8 mold, cured at 75 ℃, and then bonded to the patterned CNT chip via oxygen plasma treatment.

Layer-by-Layer (LbL) Assembly:

Prior to LbL assembly, CNT elements were treated with surfactant SDBS (Sigma: 289957-258, 10 mg/mL) in DI water via flow through microfluidic chips. A syringe pump was used to flow SDBS (3 min at 6 μL /min) through both the inlet and outlet, and devices were left overnight in surfactant solution. On the following day, continuous alternate flow (6 μL /min, 5 min) of PAH-Fluor (15 kDa, **Sigma 630217**) and SPS (70 kDa, Sigma 243051), pH 9.3, no salt with intermediate DI water rinse at pH 9.3 [6 μL /min] for 5 min. in between was performed to the desired number of bilayers. PAH-Fluor was deposited first and last. All solutions filtered through 0.22 μm filter prior to use. After LbL deposition, device must be kept wet in DI water for further use.

Prostate Specific Antigen (PSA) Capture Assay:

Prior to functionalization, an acid treatment (DI water, pH 2.5, 6 μL/min, 15 min) followed by a DI water rinse (6 μL/min, 5 min) is required. Using a glass syringe, NHS-Biotin (Sigma-Aldrich, St. Louis, MO) was introduced into the devices for 15 mins at 6 μL/min (5 mM in Dimethyl sulfoxide (DMSO), followed by incubation for 2 hr RT. Blocking Buffer (6% BSA) was then delivered at the same flow rate for 3 min and incubated for 1 hr RT. Neutravidin (Sigma-Aldrich, St. Louis, MO) (50 μg/mL) was diluted in Blocking Buffer and then administered for 3 min at the same flow rate of 6 μL/min before incubation for 1 hr at 4Cº. Next, 25 μL of Biotinylated PSA Antibody (Thermo Fisher Scientific, Waltham, MA) (4 μg/mL) was diluted in Blocking Buffer and pipetted directly into the inlet followed by a 30 min incubation at RT. Blocking Buffer incubation was performed again for 30 min at RT. Afterwards, 20 μL of Prostate Specific Antigen (Thermo Fisher Scientific, Waltham, MA) (PSA, 100 ng/mL) was pipetted directly into device followed by a 2-min incubation at RT. 20 μL of PSA Antibody (4 μg/mL) was then diluted in Blocking Buffer and pipetted directly into device, and incubated for 2 min RT before pipetting 20 μL of a biotinylated quantum-dot solution (Life Technologies, Grand Island, NY) (605 nm, 20 nM) into the device and incubating for 5 min RT. Device rinsing with PBS at 6 μL/min for 5 min is done after each step.

A Blocking Buffer (6% BSA) rinse (3 uL/min, 3 min) and incubation (RT, 1 hr) followed by incubation with quantum dots (605 nm, 20 nM) was used for the control. Quantum dots were pipetted into the device, incubated for 5 min at RT, and then rinsed with DI water (6 uL/min, 5 min). Device rinsing with PBS at 6 μL/min for 5 min is done after each step. All control devices shown in figure were first processed with layer-by-layer assembly. Additionally, a control of solely CNT element following the above protocol was performed, and yielded no signal.

The devices were scanned under fluorescent microscopy, bright field microscopy, and confocal microscopy. The capture efficiency was found by measuring the intensity of 15 50 x 50 pixel square areas in the CNT element area and the background area, averaging, and dividing the intensity data for CNT elements by the background average signal. This analysis was performed using ImageJ software.

Numerical Simulation details:

To investigate the effect of the presence of a gap on the polymer adsorption on the CNTs we developed a suitable three-dimensional numerical model. For a laminar flow of an incompressible Newtonian fluid the governing equations in this problem are given in the following set of equations, which respectively represent continuity, conservation of species in the free flow region, conservation of species in the porous region, the momentum equation in the free flow region, and the momentum equation in the porous region i.e. the extended Darcy-Brinkman equation:

$$\nabla \cdot \mathbf{u} = 0$$

$$\frac{\partial c}{\partial t} + \nabla.(c\mathbf{u}) = \nabla \cdot (D_{12}\nabla c)$$

$$\varepsilon\frac{\partial c}{\partial t} + \nabla.(c\mathbf{u}) = \varepsilon\tau D_{12}\nabla^2 c$$

$$\rho\left(\frac{\partial \mathbf{u}}{\partial t} + \mathbf{u}.\nabla\mathbf{u}\right) = -\nabla p + \mu\nabla^2\mathbf{u}$$

$$\frac{\rho}{\varepsilon}\left(\frac{\partial \mathbf{u}}{\partial t} + \frac{1}{\varepsilon}\mathbf{u}.\nabla\mathbf{u}\right) = -\nabla p + \frac{\mu}{\varepsilon}\nabla^2\mathbf{u} - \frac{\mu}{\kappa}\mathbf{u}$$

where $\mathbf{u}$, c, and p denote the velocity vector, the concentration, and the pressure field, respectively. The independent variables are the fluid density, ρ, the porosity, ε, the permeability, κ, and the binary diffusion coefficient, D_{12} . The parameter τ is the tortuosity factor which is assumed to be $\tau = \varepsilon^{1/3}$ [71]. The initial condition was zero velocity, zero relative pressure, and zero concentration. The inlet flow has a uniform velocity and concentration and the outlet flow has zero relative pressure. Since the polymer solutions are dilute, using a Newtonian model is justified.

In the above equations we assumed that the porous medium (CNT forest) is homogeneous and isotropic with a constant porosity and permeability. In addition, the binary diffusion coefficient is assumed to be constant. According to [72] anisotropic diffusivity in fibrous media is not expected when porosity is high and the particles are much smaller than the fiber diameter. We have solved the governing equations numerically using COMSOL Multiphysics 4.4 for two device designs: straight channels with a rectangular cross section of $50\mu m \times 3mm$ and $100\mu m \times 3mm$, both having a length of 6 mm and including a cylindrical porous post of height 50 μm in the center. Consequently, in one design the CNTs are touching the bottom and top walls while in the other there is a $50\mu m$ gap between the CNTs and the top wall. The model input parameters are $\varepsilon = 0.99$, $\kappa = 7.5 \times 10^{-16}\, m^2$, $D_{12} = 10^{-11}\, m^2/s$, which is in the range of data reported in [65]. The inlet flow has a velocity of $3.3 \times 10^{-4}\, m/s$ and concentration of $10mM$, based on experimental conditions. The resulting contours qualitatively represent the corresponding pattern observed in the experiments. For a quantitative comparison we need the exact binary diffusion coefficient in the porous matrix.

References

1 Guarini, K., Black, C., Milkove, K. & Sandstrom, R. Nanoscale patterning using self-assembled polymers for semiconductor applications. J. Vac. Sci. Technol. B. 2001; 19: 2784-2788 .

2 Lee, H. & Jung, G.-Y. Wafer to wafer nano-imprinting lithography with monomer based thermally curable resin. Microelectronic Engineering 2005; 77: 168-174.

3 Oh, Y., Choi, C., Hong, D., et al. Magnetically guided nano-micro shaping and slicing of silicon. Nano Letters 2012;. 12: 2045–50.

4 Aricò, A., Bruce, P., Scrosati, et al. Nanostructured materials for advanced energy conversion and storage devices. Nature Materials 2005; 4: 366-377.

5 Nazar, L. et al. Nanostructured materials for energy storage. International Journal of Inorganic Materials 2001; 3: 191-200.

6 Liu, C., Li, F., Ma, L. & Cheng, H. Advanced Materials for Energy Storage.Adv. Mater. 22, E28-E62 (2010).

7 Li, Y. & Somorjai, G. Nanoscale Advances in Catalysis and Energy Applications. Nano Letters 2010; 10: 2289-2295.

8 Ozbay, E. Plasmonics: Merging Photonics and Electronics at Nanoscale Dimensions. Science 2006; 311: 189-193.

9 Barone, P., et al. Near-infrared optical sensors based on single-walled carbon nanotubes. Nature Materials 2004; 4: 86-92.

10 Ibn-Elhaj, M. & Schadt, M. Optical polymer thin films with isotropic and anisotropic nano-corrugated surface topologies. Nature 2001; 410: 796-799.

11 Shipway, A., Katz, E. & Willner, I. Nanoparticle Arrays on Surfaces for Electronic, Optical, and Sensor Applications. Chem Phys Chem 2000. 1: 18-52.

12 Caruso, F. Nanoengineering of Particle Surfaces. Adv. Materials 2001; 13: 11-22 (2001).

13 West, J. & Halas, N. Engineered Nanomaterials for Biophotonoics Applications: Improving Sensing, Imaging, and Therapeutics. Annu. Rev. Biomed. Eng 2003;. 5: 285-292.

14 Frey, N., Peng, S., Cheng, K. & Sun, S. Magnetic nanoparticles : synthesis, functionalization, and applications in bioimaging and magnetic energy storage. Chem. Soc. Rev. 2009; 38: 2532-2542.

15 Castner, D. & Ratner, B. Biomedical surface science: Foundations to frontiers. Surface Science 2002; 500: 28-60.

16 Roach, P., Farrar, D. & Perry, C. Surface Tailoring for Controlled Protein Adsorption: Effect of Topography at the Nanometer Scale and Chemistry. J. Am. Chem. Soc. 2006; 128: 3939-3945.

17 Koo, O., Rubinstein, I. & Onyuksel, H. Role of nanotechnology in targeted drug delivery and imaging: a concise review. Nanomedicine: Nanotechnology, Biology and Medicine 2005; 1: 193-212.

18 Stensballe, A., Andersen, S. & Jensen, O. Characterization of phosphoproteins from electrophoretic gels by nanoscale Fe(III) affinity chromatography with off-line mass spectrometry analysis. Proteomics 2001; 1: 207-222.

19 Melechko, A. et al. Vertically aligned carbon nanofibers and related structures: Controlled synthesis and directed assembly. J. Appl. Phys. 2005; 97: 041301-1-041301-39.

20 Breuer, O. & Sundararaj, U. Big returns from small fibers: A review of polymer/carbon nanotube composites. Polym Compos 2004; 25(6), 630-645.

21 Jong, K. & Geus, J. Carbon Nanofibers: Catalytic Synthesis and Applications. Catalysis Reviews 2007; 42(4), 481-510.

22 Salvetat, J.-P. et al. Mechanical properties of carbon nanotubes. Applied Physics A: Materials Science & Processing 1999; 69: 252-260.

23 Ruoff, R., Qian, D. & Liu, W. Mechanical properties of carbon nanotubes: theoretical predictions and experimental measurements. Comptes Rendus Physique 2003; 4: 993-1008.

24 Yakobson, B. & Avouris, P. Mechanical Properties of Carbon Nanotubes. Top. Appl. Phys 2001;. 80: 287-327.

25 Volder, M., Tawfick, S., Baughman, R. & Hart, A. Carbon Nanotubes: Present and Future Commercial Applications. Science 2013; 339, 535-539.

26 Dresselhaus, M., Dresselhaus, G., Charlier, J., et al. Electronic, thermal and mechanical properties of carbon nanotubes. Philosophical Transactions of the Royal Society A: Mathematical, Physical and Engineering Sciences 2004; 362: 2065-2098.

27 Nihei, M. et al. Electrical Properties of Carbon Nanotube Bundles for Future Via Interconnects. Jpn. J. Appl. Phys 2005; 44: 1626-1628.

28 Ebbesen, T. et al. Electrical conductivity of individual carbon nanotubes. Nature 1996; 382: 54-56.

29 Kataura, H. et al. Optical properties of single-wall carbon nanotubes. Synthetic Metals 1999; 103: 2255-2258.

30 Liu, L., Ma, W. , and Zhang, Z., "Macroscopic Carbon Nanotube Assemblies: Preparation, Properties, and Potential Applications", Small 2011; 7(11): 1504–1520.

31 Schnorr, J. M., and Swager, T. M., "Emerging Applications of Carbon Nanotubes," Chemistry of Materials 2011; 23(3): 646–657.

32 Chen, G., et al. Nanoporous micro-element arrays for particle interception in microfluidic cell separation. Lab Chip 2012; 12: 3159-3167.

33 Fachin, F., Chen, G., Toner, M. & Wardle, B. Integration of Bulk Nanoporous Elements in Microfluidic Devices With Application to Biomedical Diagnostics. J. Microelectromech. Syst. 2011; 20: 1428-1438.

34 Decher, G. Fuzzy Nanoassemblies: Toward Layered Polymeric Multicomposites. Science 1997; 277: 1232-1237.

35 Michel, M. et al. Deposition Mechanisms in Layer-by-Layer or Step-by-Step Deposition Methods: From Elastic and Impermeable Films to Soft Membranes with Ion Exchange Properties. ISRN Materials Science 2012; 2012: 1-13.

36 Tang, Z., et al. Biomedical Applications of Layer-by-Layer Assembly: From Biomimetics to Tissue Engineering. Adv. Mater. 2006; 18: 3203–3224.

37 Monge, C., Almodovar, J. Boudou, T. et al. Spatio-Temporal Control of LbL Films for Biomedical Applications: From 2D to 3D. Advanced Healthcare Materials 2015; 4(6): 811-830.

38 Richardson, J.J., Björnmalm, M., Caruso, F. Technology-driven layer-by-layer assembly of nanofilms. Science 2015; 348: 2491-1-2491-11.

39 Skorb, E., et al. Layer-by-Layer Approach for Design of Chemical Sensors and Biosensors. Current Organic Chemistry 2015; 19(12): 1097-1116.

40 Costa, R. R., Mano, J. F. Polyelectrolyte multilayered assemblies in biomedical technologies. Chemical Society Reviews 2014; 43(10): 3453-3479.

41 Ariga, K., Lvov, Y.M., Kawakamai, K., et al. Layer-by-layer assembled shells for drug delivery. Advanced Drug Devliery Reviews 2011; 63(9): 762-771.

42 DeRocher, J., Mao, P., Han, J., et al. Layer-by-Layer Assembly of Polyelectrolytes in Nanofluidic Devices. Macromolecules 2010; 43: 2430-2437.

43 Kim, J. Y.; DeRocher, J. P.; Mao, et al. Formation of Nanoparticle-Containing Multilayers in Nanochannels via Layer-by-Layer Assembly. Chem. Mater. 2010; 22: 6409-6415.

44 Wang, Y., Alexandra, S.A., Caruso, F. Template Synthesis of Nanostructured Materials via Layer-by-Layer Assembly. Chem. Mater. 2008; 3: 848-858.

45 Azzaroni, O., Lau, K.H. Aaron. Layer-by-layer assemblies in nanoporous templates: nano-organized design and applications of soft nanotechnology. Soft Matter 2011; 19: 8709-8724.

46 Komatsu, T. Protein-based nanotubes for biomedical applications. Nanoscale 2012; 4(6): 1910-1918.

47 Sung, W.C. et al. Long-term affinity modification on poly(dimethylsiloxane) substrate and its application for ELISA analysis. Anal. Chem. 2008; 80: 1529-1535.

48 Weng, C.H. et al. A suction-ype microfluidic immunosensing chip for rapid detection of the dengue virus. Biomed. Microdevices 2011; 13: 585-595.

49 Kirchof, K. et al. Polyelectrolyte multilayers generated in a microfluidic device with pH gradients direct adhesion and movement of cells. Lab Chip 2011; 11: 3326-3335.

50 Barker, S., Ross, D., Tarlov, M., Gaitan, M. & Locascio, L. Control of Flow Direction in Microfluidic Devices with Polyelectrolyte Multilayers. Anal. Chem. 2000; 72: 5925-5929.

51 Lee , J. et al. Impact of carbon nanotube length on electron transport in aligned carbon nanotube networks. Appl. Phys Letters 2015; 106: 053110-1-053110-5.

52 Stein, I.Y., et al. Exohedral Physisorption of Ambient Moisture Scales Non-monotonically with Fiber Proximity in Aligned Carbon Nanotube Arrays. ACS Nano 2014; 8(5): 4591-4599.

53 Qin, D., Xia, Y. & Whitesides, G. Soft lithography for micro- and nanoscale patterning. Nat Protocol 2010; 5(3): 491-502.

54 Vaisman, L., Wagner, H. & Marom, G. The role of surfactants in dispersion of carbon nanotubes. Advances in Colloid and Interface Science 2006; 37(46): 128-130.

55 Bystrzejewski, M. et al. Dispersion and diameter separation of multi-wall carbon nanotubes in aqueous solutions. Journal of Colloid and Interface Science 2010; 345: 138-142.

56 Ma, P.-C., et al. Dispersion and functionalization of carbon nanotubes for polymer-based nanocomposites: A review. Composites Part A: Applied Science and Manufacturing 2010; 41: 1345-1367.

57 Itano, K.; Choi, J. Y.; Rubner, M. F. Mechanism of the pH-induced discontinuous swelling/deswelling transitions of poly(allylamine hydrochloride)-containing polyelectrolyte multilayer films. Macromolecules 2005; 38(8): 3450-3460.

58 Lichter, J. A., and Rubner, M.F. Polyelectrolyte Multilayers with Intrinsic Antimicrobial Functionality: The Importance of Mobile Polycations. Langmuir 2009; 25(13): 7686-7694.

59 Polak, R. et al. Optimization of Amine-Rich Multilayer Thin Films for the Capture and Quantification of Prostate-Specific Antigen. Langmuir 2015; 31(19): 5479-5488.

60 Kim, S.J., Han, J. Self-Sealed Vertical Polymeric Nanoporous-Junctions for High-Throughput Nanofluidic Applications. Analytical Chemistry 2008; 80: 3507-3511.

61 Stuart, MA Cohen, C. W. Hoogendam, and A. De Keizer. Kinetics of polyelectrolyte adsorption. Journal of Physics: Condensed Matter 1997; 9(37): 7767.

62 Fogler, H. Scott. Elements of chemical reaction engineering. 3rd ed. Upper Saddle River: Prentice Hall, 1999.

63 Tamayol, Ali, and Majid Bahrami. Transverse permeability of fibrous porous media. Phys. Rev. E 2011; 84(4): 046314-1-046314-9.

64 Ferreira, M., and M. F. Rubner. Molecular-level processing of conjugated polymers.1Layer-by-layer manipulation of conjugated polyions. Macromolecules 1995; 28(21): 7107-7114.

65 Shahsavari, Setareh, and Gareth McKinley. "Interception efficiency in flow of power-law fluids past confined porous bodies." Bulletin of the American Physical Society 2014; 59.

66 Lilja, H., Ulmert, D. & Vickers, A. Prostate-specific antigen and prostate cancer: prediction, detection and monitoring. Nat Rev Cancer 2008; 8: 268- 278.

67 Zhang, W. D., et al. Growth of vertically aligned carbon-nanotube array on large area of quartz plates by chemical vapor deposition. Applied Physics A: Materials Science & Processing 2001; 74: 419-422.

68 Terrado et al. Aligned carbon nanotubes grown on alumina and quartz substrates by a simple thermal CVD process. Diamond and Related Materials 2006; 15: 1059-1063.

69 E. J. García, A. J. Hart, B. L. Wardle, and A. H. Slocum. Fabrication of composite microstructures by capillarity-driven wetting of aligned carbon nanotubes with polymers. Nanotechnology 2007; 18: 1-11.

70 A. J. Hart and A. H. Slocum. Rapid growth and low-mediated nucleation of millimeter-scale aligned carbon nanotube structures from a thin-film catalyst. J. Phys. Chem. B 2006; 110(16): 8250–8257.

71 Boudreau, Bernard P. The diffusive tortuosity of fine-grained unlithified sediments. Geochimica et Cosmochimica Acta 1996; 60(16): 3139-3142.

72 Stylianopoulos, Triantafyllos, et al. Diffusion anisotropy in collagen gels and tumors: the effect of fiber network orientation. Biophysical Journal 2010; 99(10): 3119-3127.